

Physical entanglements mediate coherent motion of the active topological glass confined within a spherical cavity

Iurii Chubak,^{1,2,*} Stanard Mebwe Pachong,^{3,†} Kurt Kremer,^{3,‡} Christos N. Likos,^{1,§} and Jan Smrek^{1,¶}

¹*Faculty of Physics, University of Vienna, Boltzmannngasse 5, A-1090 Vienna, Austria*

²*Sorbonne Université CNRS, Physico-Chimie des électrolytes et Nanosystèmes Interfaciaux, F-75005 Paris, France*

³*Max Planck Institute for Polymer Research, Ackermannweg 10, 55128 Mainz, Germany*

Motivated by chromosomes enclosed in nucleus and the recently discovered active topological glass, we study a spherically confined melt of long nonconcatenated active polymer rings. Without activity, the rings exhibit the same average large-scale conformational properties as chromatin fiber. Upon activating consecutive monomer segments on the rings, the system arrives at a glassy steady state due to activity-enhanced topological constraints. The latter generate coherent motions of the system, however the resulting large-scale structures are inconsistent with the fractal globule model. We observe microphase separation between active and passive segments without systematic trends in the positioning of active domains within the confining sphere. We find that tank-treading of active segments along the ring contour enhances active-passive phase separation in the state of active topological glass when both diffusional and conformational relaxation of the rings are significantly suppressed. Finally, although the present model of partly-active rings is not compatible with the large-scale chromatin organization, our results suggest that the activity-enhanced entanglements that result in facilitated intra- and inter-chromosomal contacts might be relevant for chromatin structure at smaller scales.

The active topological glass (ATG) is a state of matter composed of polymers with fixed, circular, unknotted topology, that vitrifies upon turning a block of monomers within the polymers active and fluidizes reversibly [1]. Unlike classical glasses, where the transition is driven by temperature or density, the ATG results from physical, tight, threading entanglements, generated and maintained by the activity of polymer segments. The activity acting on the ring segments, modeled here as stronger-than-thermal fluctuations, triggers a directed snake-like motion that overcomes entropically unfavorable states and results in significantly enhanced inter-ring threading [2]. A topological glass is hypothesized to exist also in equilibrium solutions of sufficiently long ring polymers, where rings naturally thread (pierce through each other's opening). However, the conjectured critical ring length is currently beyond the experimental or computational reach [3–5]. Although the ATG exhibits accessible critical ring lengths, a formidable challenge in simulating these systems stems from large system sizes that are necessary to avoid self-threading of significantly elongated partly-active rings due to periodic boundary conditions [1]. To overcome this difficulty, a much smaller system confined to an impenetrable cavity can be simulated.

However, in analogy to classical glasses, where the confinement affects the vitrification mechanism and shifts the glass transition temperature in comparison to the bulk value [6, 7], it is necessary to ask the question whether the ATG, the existence of which relies on highly extended configurations that promote inter-molecular entanglement, can exist in such a strong confinement at all.

Besides the ATG, the confined melt of uncrossable polymer rings with active segments has an interesting biological connection. The *equilibrium* melt of rings

exhibits conformational properties consistent with the large-scale, population-averaged properties of chromatin fiber in the interphase nuclei of higher eukaryotes [8–10]. In detail, the territorial segregation of distinct chains, the critical exponents $\nu = 1/3$ and $\gamma \simeq 1.1$ governing the scaling of the gyration radius $R(s) \sim s^\nu$ and the probability of end-contacts $P(s) \sim s^{-\gamma}$ of a segment of length s respectively, coincide for the two systems and characterize the so-called fractal (crumpled) globule conformations [11]. However, similarly to partly active rings, chromatin is out of equilibrium on smaller scales as well. Various processes, such as transcription or loop extrusion inject energy into the system by the action of respective molecular machines on the chromatin fiber. Fluorescence experiments [12] and the related analytical theory [13] suggest that some active events at small scales render fluctuations with thermal spectrum at an effective temperature about twice higher than the ambient one. While *not* aiming at a faithful biological representation of the chromatin, we question whether the ATG is consistent with the fractal globule model, since both of the latter represent some aspects of the chromatin conformations in space and time.

Motivated by both the question on the existence of the confined ATG and the question on the consistency with the fractal globule model of chromatin, here we explore the static and dynamic properties of long, confined, partly-active, nonconcatenated rings in melt. We find that essentially the same phenomenon of the ATG formation is present in confined systems with a small number of polymer chains. The ability to simulate longer rings than in the bulk, allows us to assess in more detail the conformational and scaling properties of the chains in the non-equilibrium glassy state. We discover that

intermediate-length ring segments feature conformations consistent with a self-avoiding random walk ($\nu = 0.588$, $\gamma = 1.75$). While the territorial structure of the fractal globule is clearly distorted, we observe active-passive microphase-separated domains and large-scale correlated motion arising from the glassy phase due to the activity-induced topological constraints. In contrast to chromatin models in [14, 15], where the large-scale dynamical coherence arises from explicit interaction potentials or crosslinks, here we show that the activity-induced entanglement can mediate the correlated motion as well. Finally, we observe tank-treading of active segments along the ring contour in the glassy state that acts to enhance active-passive phase separation when both chain diffusion and its conformational rearrangements are suppressed.

We start from a well equilibrated sample of $M = 46$ rings each of length N obtained in [10] ($N = 200, 400, 800$ and 1600 that corresponds to chain entanglement lengths of $Z = N/N_e \in [7 - 57]$), the longest being four times longer than the system in [1]. We impose the activity on a consecutive segment of length $N/8$ by coupling it to a (hot) thermostat with temperature $T_h = 3T_c$, where T_c is the temperature of passive (cold) monomers. We use the well-established polymer model [16–18], described in detail in the Supporting Information (SI). The radius R of the confining sphere, which is modeled as a smooth structureless purely repulsive barrier (SI), is fixed by the total monomer density $\rho = 0.85\sigma^{-3}$ for all systems. Typically, R is about 2.5 – 2.7 times larger than the equilibrium radius of gyration of the confined chains (Tab. S3).

When the activity is switched on, after about $10^5\tau$, τ being the microscopic time of the model (see Section S1 in the SI), the chains start to expand from their equilibrium sizes until they reach a steady state after $(2 - 3) \cdot 10^6\tau$. The time of the onset of the chain stretching does not significantly depend on N because it is related to local threading constraints. The steady state is characterized by a significantly enhanced mean-square radius of gyration R_g^2 (see snapshot of a chain in Fig. 1d and more in Fig. S1 in the SI, time evolution of R_g^2 in Fig. 1a and Tab. S1 for shape parameter comparison). In comparison to the bulk [1], the confined rings are significantly less expanded in terms of R_g and the ratio of the two biggest eigenvalues of the gyration tensor (Fig. S2a and compare Tab. S1 to Tab. S2 of $N = 400$). Nevertheless, the conformations are mostly doubly-folded and the change in the shape parameters is due to “reflections” from the walls. This can be seen in the mean-square internal distance of the longest rings being non-monotonic function of the contour length (Fig. S2b). In comparison to equilibrium (Tab. S3), the rings are highly stretched and exhibit self-avoiding walk-like scaling at intermediate distances (Fig. S2c) with a consistent scaling of the contact probability with the exponent γ close to 1.75 (Fig. S2d) [9] and a plateau at largest distances, signifying the loss of correlation due to reflections of rings from

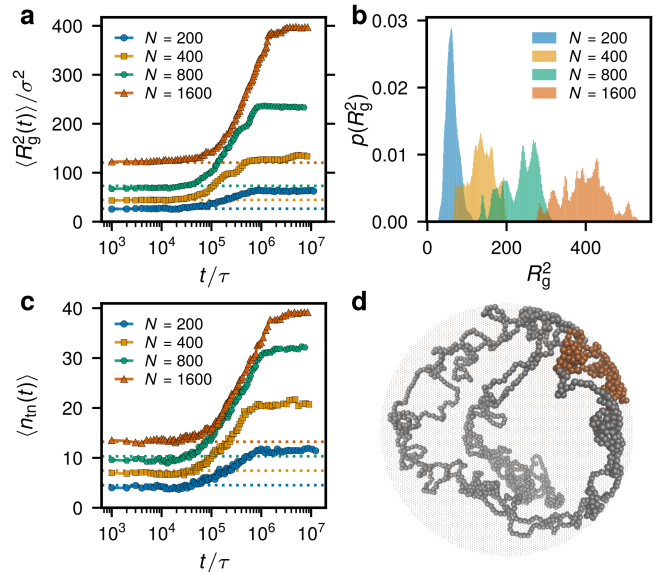


FIG. 1. **Conformational properties.** **a**, Evolution of the ring’s R_g^2 after the activity onset at $t = 0$ for systems with different N . **b**, Distribution of R_g^2 in the steady state. **c**, Evolution of the mean number of threaded neighbors (see Section S2 in the SI). **d**, Conformation of a partly-active ring with $N = 1600$ at the end of the simulation run. In **a** and **c**, the dashed lines of the respective color indicate the values in equivalent equilibrium ring melts [10].

the walls. The stretched conformations and the different profile of the contact probability signifies the loss of the original crumpled globule characteristics. The stretching due to the snake-like motion is caused by strong dynamic asymmetry between the active and the passive segments, apparently triggered by non-equilibrium phase separation [1, 2, 19]. The dynamics of the mutual ring threading coincides with the stretching dynamics and exhibits markedly enhanced numbers of threaded neighbors n_{tn} by a single ring in the steady state in comparison to equilibrium (Fig. 1c), as we showed by analyzing piercings of rings through other rings’ minimal surfaces (SI) [1, 10, 20–22]. Interestingly, the number of threaded neighbors is the same as for the active topological glass in the bulk, despite the different ring shape (compare Tab. S1 and S2). For the longest rings, each ring practically threads all the other rings in the system. Although this does not hold for the shorter rings, their dynamic behavior is comparable, as detailed below.

The steady states exhibit a rugged distribution of R_g^2 (Fig. 1b), despite averaging over about $10^7\tau$, time that is more than one order of magnitude above the equilibrium diffusion times for $N \leq 800$. This shows that the individual chains are not able to change their conformations significantly, being frozen essentially in the same state, and points to a non-ergodic behavior. When averaged over 10 independent runs, a smoother distribution is recovered, as shown for $N = 200$ in Fig. 1b.

The chosen model parameters trigger active-passive (micro)phase separation in all the systems [2, 19, 23]. We track the degree of phase separation by the order parameter $\Phi(t) = x(t)/x(0) - 1$, where $x(t)$ is the number fraction of inter-chain like-particles in a $r_c = 2^{1/6}\sigma$ neighborhood of a given monomer at a given time t , averaged over monomers (Fig. 2a). The initial increase of the order parameter precedes the ring stretching and threading dynamics, supporting the conjecture in [2] that the separation tendency is a precursor of the formation of the glass. The phase separation is dynamic in nature, showing intervals of a single mostly-hot region, but also subsequent dissociation into several hot blobs (Supporting Video 1) reminiscent of the dynamics of activity-driven colloidal crystals [24]. When the shape properties arrive at a steady state, there are several hot blobs (Fig. 2b) and we still observe them occasionally exchanging hot particles. As described below, these are the consequence of a rare tank treading motion of some of the rings, by which the hot segment joins the hot phase without changing the overall shape of the ring and the system as a whole. The radial density distribution of the hot monomers averaged over 10 different runs for $N = 200$ displays confinement induced layering at the wall as in equilibrium [10], and displays another broad maximum around $R/2$ (Fig. 2c). However, the analysis of single runs for $N = 200$ and for other N shows that the positioning of hot monomers is history-dependent, arrested by the topological constraints, and allows for both, internal or peripheral locations (Fig. 2d) in contrast to preference for central locations of active monomers in a different polymer model in [25].

In Fig. 3 we report dynamical and relaxation properties of rings in the system with $N = 200$ (averaged over 10 independent runs). We focus on the late stage dynamics by discarding the initial period of length $3 \cdot 10^6 \tau$, where major configurational rearrangements occur. The late-stage (steady-state) dynamics of the ring's center of mass, $g_3(t)$, (Eq. (S4) in the SI), is much slower than in the equilibrium case [10], with negligible relative displacements between the rings $g_{3,rel}(t)$, (Eq. (S5)) as shown in Fig. 3a. Importantly, the latter quantity is invariant under overall constant global rotations and shows that the relative ring's motion essentially stalls. The systems with longer rings display the same behavior. In confined systems, $g_3(t)$, saturates at a constant value; for the rings with $N = 200$, we find that $g_3(t \rightarrow \infty) \approx 0.4R^2$, which is about two times smaller than in the equivalent equilibrium case (Fig. 3a). This arises mostly from extremely elongated and practically frozen rings conformations, due to which the exploration of the available volume is significantly suppressed (Supporting Video 2).

We characterize the ring structural relaxation by considering the terminal autocorrelation function (TACF) $\langle \mathbf{u}(t) \cdot \mathbf{u}(0) \rangle$, where $\mathbf{u}(t)$ is the unit vector connecting two monomers separated by contour distance $N/2$, and the

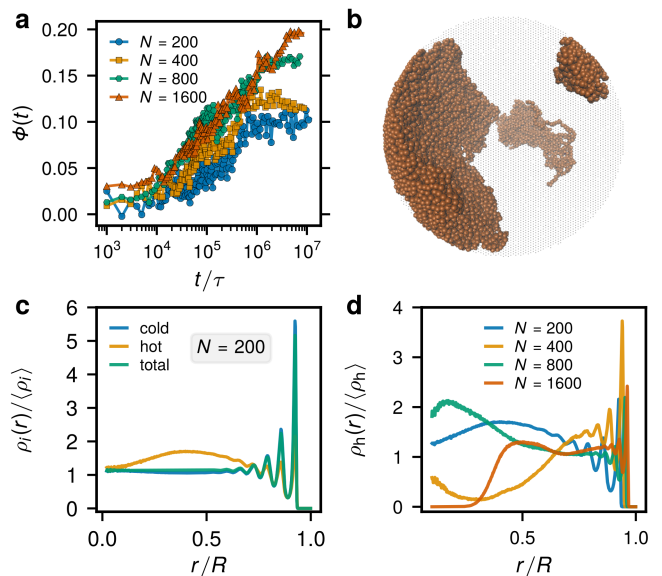


FIG. 2. **Phase segregation.** **a**, Time evolution of the order parameter $\Phi(t)$. **b**, Phase-segregated regions of hot monomers (cold not shown for clarity) for the system with $N = 1600$. **c**, Radial distribution of cold (blue), hot (yellow), and all (green) monomers within the enclosing sphere for the system with $N = 200$ (averaged over 10 independent runs). **d**, Radial distributions of hot monomers.

average is taken over all such monomer configurations within a ring and time [18, 26]. The full decorrelation time of the TACF ($\approx 6 \cdot 10^5 \tau$) is about three times longer than in the counterpart equilibrium case (Fig. 3b). In the steady state, the rings are found in a heavily threaded arrangement with their configurations being essentially frozen, as evidenced by the static properties. Since in the steady state the relative ring displacements are marginal (Fig. 3a), $\langle \mathbf{u}(t) \cdot \mathbf{u}(0) \rangle$ can decorrelate either through internal conformational ring relaxation or collective system rotations.

In what follows, we show that the main pathway that contributes to the decorrelation of the TACF are correlated, stochastic rotations of the whole system. The other possible decorrelation mechanism is the internal ring rearrangements, caused by the local explorations of the hot segments or tank treading motion. To show that these do not dominate, we show in Fig. 3c that the normalized autocorrelation function for the ring's R_g^2 , $C(t)$, decorrelates at a much later time ($\approx 2 \cdot 10^6 \tau$) and features a three decades long logarithmic decay. This contrasts with the equilibrium behavior, where both structural quantities R_g^2 and $\langle \mathbf{u}(t) \cdot \mathbf{u}(0) \rangle$ decorrelate at about the same time (yellow curves in Fig. 3b and Fig. 3c). Although the size of the rings remains essentially the same during the TACF relaxation, there remains a possibility of tank treading motion that can significantly impact the TACF decorrelation but keep the overall size given by R_g fixed. As highlighted in Fig. 3d, the tank treading,

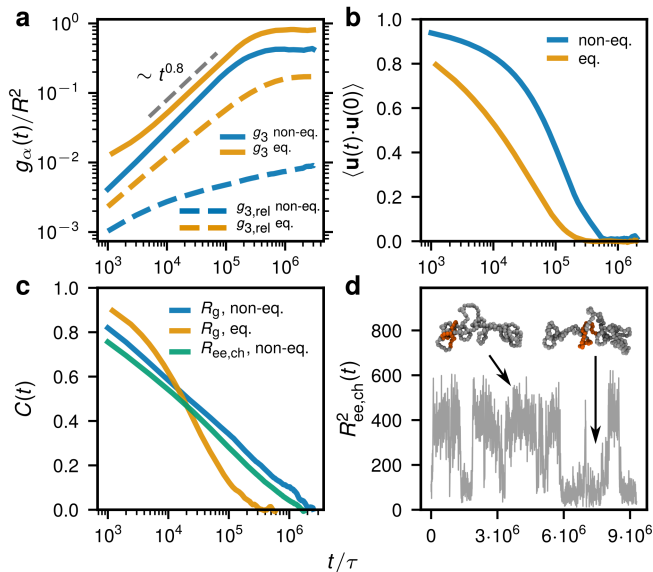


FIG. 3. **Dynamics and relaxation.** Comparison of the non-equilibrium system (blue) with the equilibrium (yellow). **a**, Mean-square displacements of the ring’s center of mass g_3 normalized by the squared sphere’s radius R^2 of $N = 200$ (solid lines). The relative mean-square displacement $g_{3,rel}(t)$ (dashed). **b**, Terminal autocorrelation function. **c**, Normalized autocorrelation function for R_g^2 . For comparison the autocorrelation of the squared “end-to-end” (i.e. between an active and a passive monomer separated by segment length $N/2$) distance $R_{ee,ch}^2$ is shown (green). In all cases we subtract the mean value squared and normalize the autocorrelation functions to unity at time zero. **d**, Time dependence of $R_{ee,ch}^2(t)$ for one of the rings illustrates tank treading motion.

a tangential motion of the hot segment along the ring’s contour, is indeed observed. Thus, such a mechanism can enhance active-passive phase separation when both diffusional and conformational relaxation of polymers is not possible. We show that the tank treading does not significantly impact the terminal relaxation by computing the autocorrelation function for the squared end-to-end distance $R_{ee,ch}^2$ between a hot and a cold monomer contour-wise $N/2$ apart (Fig. 3c). Although it decorrelates slightly faster than the one for R_g^2 , its relaxation time is still much larger than that of the TACF. Therefore, collective, stochastic rotations provide the dominant contribution to the TACF decorrelation, whereas its relaxation time scale can be used as an estimate for rotational diffusion time (the presence of such global, correlated rotations is visible in both Supporting Videos). Global rotations lead to correlated particle displacements as detailed by computing the spatio-temporal correlation function (Section S5 in the SI). Finally, such stochastic rotations can also arise spontaneously in confined equilibrium systems coupled to a Langevin thermostat (see discussion in the SI).

Let us now turn to a discussion of a possible connection

of the large correlated motions (rotational diffusion) in ATG and coherent motion of chromatin on micron scale, observed in [12, 27], interpreted also as rotations of the nucleus interior [28]. In the context of chromatin, many different mechanisms can cause large correlated motions [14, 15, 25, 29–32]. The works [14, 15, 30] focus on the spatio-temporal correlations in the dynamics. While the first one uses the thermal-like model of activity, the latter two investigate the effects of active force dipoles. These are coupled with hydrodynamic interaction in [30], while in [15], the active force dipoles act on highly crosslinked chromatin connected to deformable lamina. Note that explicit bonds are used in [15, 25, 29], which maintain the compact chromatin state in contrast to fractal globule model, where it arises from the uncrossability of the chains. All the works [14, 15, 30] find large-scale correlated motions, but of different origins. In [14], the correlated domains coincide with the micro-phase separated domains due to preferential intra-domain interaction, and the activity opposes the coherence, similarly to [31]. Non-monotonic dependence of the correlation length on time lag has been observed [12, 27]; it is not clear if it is a general phenomenon (Fig. 2 in [27]) and in contrast to [14], the coherence of the motion even at short time lags is larger for the active systems [12, 27]. The correlated motion in [30] comes from the coupling of the hydrodynamic flow due to contractile motors and the nematic ordering of the chromatin fiber (not yet observed), with no discernible effect of local topology (unknottedness) of the conformation. The contractile motor activity in [15] generates the correlated motion as a result of a high number of crosslinks between chromatin fiber, and is even enhanced when more crosslinks are used with a deformable nuclear envelope. Last but not least, apart from the role of activity in correlated motions, other, passive mechanisms are possible [33, 34]. The latter work also highlights glassy features of the chromatin dynamics, such as dynamic heterogeneity. Here we show yet another mechanism giving rise to a correlated motion, namely by activity-induced topological interactions that entangle neighboring domains that subsequently have to move in a correlated fashion.

Despite the similarity of the coherent motion (and other dynamic features [1, 35–37]) of the ATG and chromatin, based on the conformational data ($\nu = 0.588$, $\gamma = 1.75$), we conclude that the ATG in the present form is inconsistent with the chromatin large-scale conformational data and the fractal globule model ($\nu = 1/3$, $\gamma \simeq 1.1$). The conflict of dynamical and large-scale conformational properties is, however, a persistent issue also in other models that aim at elucidating the physical mechanisms rather than the capturing the conformational details [30]. More work is necessary to conclude if other types of topological glass (dynamic correlations arising from entanglements) can be consistent with fractal globule. One option opens up at smaller length scales

(below 1Mbp, which roughly corresponds to 10 beads of our largest system), where the chromatin fiber has non-trivial topology (due to cohesin mediated loops) [38] and features less compact statistics [39, 40]. Simulations with finer resolution and diverse distribution of the active segments would be necessary to give a satisfactory answer. A notable work in this context, [14], use active sites distributed along the polymer according to the epigenetic information of a given chromosome that is modelled as an uncrossable chain with initially fractal-globule large-scale conformational properties. However, the work does not report entanglements or conformational changes of the active segments. Despite some active segments being long (20-80 beads), the relatively lower density, in comparison to ours, and a differential interaction of the active and the inactive chromatin types could suppress or obscure the activity-driven conformational changes we report here. This could be also the reason why the work [14] does not observe the correlation length to depend on the activity level at short times as reported in experiments [12, 27]. Simulations with more accurate chromatin topology or experiment that would trace the chromatin type in 3D simultaneously with dynamics might elucidate the coherence mechanism.

From the materials research perspective, our work shows that the ATG can be efficiently explored at a significantly reduced computational costs in confinement. We characterized the chain static properties and discovered the tank treading relaxation mechanism that, however, does seem to affect the glass stability, but only the phase-separation properties. More detailed understanding of the topological constraints maintaining the ATG stability should be gained in future to experimentally synthesize ATG and fully characterize this novel dynamical transition.

ASSOCIATED CONTENT

The Supporting Information is available free of charge at [link to be inserted].

Additional details on the employed polymer model (Section S1); threading detection (Section S2); conformational properties of the rings (Figures S1 and S2, Tables S1-S3); mean-square displacements (Section S4); spatio-temporal correlations in the systems (Figure S3).

ACKNOWLEDGMENTS

We are thankful to R. Barth and H.-P. Hsu for fruitful discussions. JS acknowledges support from the Austrian Science Fund (FWF) through the Lise-Meitner Fellowship No. M 2470-N28. This work has been supported by the European Research Council under

the European Union’s Seventh Framework Programme (FP7/2007-2013)/ERC Grant Agreement No. 340906-MOLPROCOMP. IC acknowledges Mobility Fellowship provided by the Vienna Doctoral School in Physics (VDSP). The authors would like to acknowledge networking support by the COST Action CA17139. We are grateful for a generous computational time at Vienna Scientific Cluster and Max Planck Computing and Data Facility. This research was supported in part by the National Science Foundation under Grant No. NSF PHY-1748958 and NIH Grant No. R25GM067110. JS and KK acknowledge the program “Biological Physics of Chromosomes” KITP UCSB, 2020, for providing a discussion forum this work benefited from.

NOTES

The authors declare no competing financial interest.

DATA AVAILABILITY

The relevant data sets generated and/or analyzed in the current study are available from the corresponding authors on reasonable request.

* iurii.chubak@univie.ac.at; Joint first author

† pachong@mpip-mainz.mpg.de; Joint first author

‡ kremer@mpip-mainz.mpg.de

§ christos.likos@univie.ac.at

¶ jan.smrek@univie.ac.at

- [1] J. Smrek, I. Chubak, C. N. Likos, and K. Kremer, Active topological glass, *Nat. Commun.* **11**, 26 (2020).
- [2] I. Chubak, C. N. Likos, K. Kremer, and J. Smrek, Emergence of active topological glass through directed chain dynamics and nonequilibrium phase segregation, *Phys. Rev. Research* **2**, 043249 (2020).
- [3] D. Michieletto and M. S. Turner, A topologically driven glass in ring polymers, *Proc. Natl. Acad. Sci. U.S.A* **113**, 5195 (2016).
- [4] D. Michieletto, N. Nahali, and A. Rosa, Glassiness and heterogeneous dynamics in dense solutions of ring polymers, *Phys. Rev. Lett.* **119**, 197801 (2017).
- [5] L. Wei-Chang and M. S. Turner, The topological glass in ring polymers, *EPL* **102**, 58005 (2013).
- [6] C. L. Jackson and G. B. McKenna, The glass transition of organic liquids confined to small pores, *J. Non-Cryst. Solids* **131-133**, 221 (1991).
- [7] P. Pissis, D. Daoukaki-Diamanti, L. Apekis, and C. Christodoulides, The glass transition in confined liquids, *J. Phys. Condens. Matter* **6**, L325 (1994).
- [8] A. Rosa and R. Everaers, Structure and dynamics of interphase chromosomes, *PLOS Comput. Biol.* **4**, 1 (2008).
- [9] J. Halverson, J. Smrek, K. Kremer, and A. Grosberg, From a melt of rings to chromosome territories: The role

- of topological constraints in genome folding, *Rep. Prog. Phys.* **77**, 022601 (2014).
- [10] S. M. Pachong, I. Chubak, K. Kremer, and J. Smrek, Melts of nonconcatenated rings in spherical confinement, *J. Chem. Phys.* **153**, 064903 (2020).
- [11] A. Y. Grosberg, S. Nechaev, and E. Shakhnovich, The role of topological constraints in the kinetics of collapse of macromolecules, *J. Phys. France* **49**, 2095 (1988).
- [12] D. W. A. Zidovska and T. Mitchson, Micron-scale coherence in interphase chromatin dynamics, *Proc. Natl. Acad. Sci. U.S.A* **110**, 1555 (2013).
- [13] R. Bruinsma, A. Y. Grosberg, Y. Rabin, and A. Zidovska, Chromatin hydrodynamics, *Biophys. J.* **106**, 1871 (2014).
- [14] L. Liu, G. Shi, D. Thirumalai, and C. Hyeon, Chain organization of human interphase chromosome determines the spatiotemporal dynamics of chromatin loci, *PLOS Comput. Biol.* **14**, 1 (2018).
- [15] K. Liu, A. E. Patteson, E. J. Banigan, and J. M. Schwarz, Dynamic nuclear structure emerges from chromatin cross-links and motors, *Phys. Rev. Lett.* **126**, 158101 (2021).
- [16] K. Kremer and G. S. Grest, Dynamics of entangled linear polymer melts: A molecular-dynamics simulation, *J. Chem. Phys.* **92**, 5057 (1990).
- [17] J. D. Halverson, W. B. Lee, G. S. Grest, A. Y. Grosberg, and K. Kremer, Molecular dynamics simulation study of nonconcatenated ring polymers in a melt. I. Statics, *J. Chem. Phys.* **134**, 204904 (2011).
- [18] J. D. Halverson, W. B. Lee, G. S. Grest, A. Y. Grosberg, and K. Kremer, Molecular dynamics simulation study of nonconcatenated ring polymers in a melt. II. Dynamics, *J. Chem. Phys.* **134**, 204905 (2011).
- [19] J. Smrek and K. Kremer, Small activity differences drive phase separation in active-passive polymer mixtures, *Phys. Rev. Lett.* **118**, 098002 (2017).
- [20] J. Smrek and A. Y. Grosberg, Minimal surfaces on unconcatenated polymer rings in melt, *ACS Macro Lett.* **5**, 750 (2016).
- [21] J. Smrek, K. Kremer, and A. Rosa, Threading of unconcatenated ring polymers at high concentrations: Double-folded vs time-equilibrated structures, *ACS Macro Lett.* **8**, 155 (2019).
- [22] A. Rosa, J. Smrek, M. S. Turner, and D. Michieletto, Threading-induced dynamical transition in tadpole-shaped polymers, *ACS Macro Lett.* **9**, 743 (2020).
- [23] J. Smrek and K. Kremer, Interfacial properties of active-passive polymer mixtures, *Entropy* **20** (2018).
- [24] J. Palacci, S. Sacanna, A. P. Steinberg, D. J. Pine, and P. M. Chaikin, Living crystals of light-activated colloidal surfers, *Science* **339**, 936 (2013).
- [25] N. Ganai, S. Sengupta, and G. I. Menon, Chromosome positioning from activity-based segregation, *Nucleic Acids Res.* **42**, 4145 (2014).
- [26] D. G. Tsalikis and V. G. Mavrantzas, Size and diffusivity of polymer rings in linear polymer matrices: The key role of threading events, *Macromolecules* **53**, 803 (2020).
- [27] H. A. Shaban, R. Barth, and K. Bystricky, Formation of correlated chromatin domains at nanoscale dynamic resolution during transcription, *Nucleic Acids Res.* **46**, e77 (2018).
- [28] H. Strickfaden, A. Zunhammer, S. van Koningsbruggen, D. Köhler, and T. Cremer, 4D chromatin dynamics in cycling cells: Theodor boveri's hypotheses revisited, *Nucleus* **1**, 284 (2010).
- [29] A. Agrawal, N. Ganai, S. Sengupta, and G. I. Menon, Chromatin as active matter, *J. Stat. Mech.: Theory Exp.* **2017**, 014001 (2017).
- [30] D. Saintillan, M. J. Shelley, and A. Zidovska, Extensile motor activity drives coherent motions in a model of interphase chromatin, *Proc. Natl. Acad. Sci. U.S.A* **115**, 11442 (2018).
- [31] J. Nuebler, G. Fudenberg, M. Imakaev, N. Abdennur, and L. A. Mirny, Chromatin organization by an interplay of loop extrusion and compartmental segregation, *Proc. Natl. Acad. Sci. U.S.A* **115**, E6697 (2018).
- [32] F. G. Woodhouse and R. E. Goldstein, Spontaneous circulation of confined active suspensions, *Phys. Rev. Lett.* **109**, 168105 (2012).
- [33] M. Di Pierro, D. A. Potoyan, P. G. Wolynes, and J. N. Onuchic, Anomalous diffusion, spatial coherence, and viscoelasticity from the energy landscape of human chromosomes, *Proc. Natl. Acad. Sci. U.S.A* **115**, 7753 (2018).
- [34] G. Shi, L. Liu, C. Hyeon, and D. Thirumalai, Interphase human chromosome exhibits out of equilibrium glassy dynamics, *Nat. Commun.* **9**, 3161 (2018).
- [35] C.-H. Chuang, A. E. Carpenter, B. Fuchsova, T. Johnson, P. de Lanerolle, and A. S. Belmont, Long-range directional movement of an interphase chromosome site, *Curr. Biol.* **16**, 825 (2006).
- [36] R. Nagashima, K. Hibino, S. Ashwin, M. Babokhov, S. Fujishiro, R. Imai, T. Nozaki, S. Tamura, T. Tani, H. Kimura, et al., Single nucleosome imaging reveals loose genome chromatin networks via active RNA polymerase II, *J. Cell Biol.* **218**, 1511 (2019).
- [37] S. Leidescher, J. Ribisel, S. Ullrich, Y. Feodorova, E. Hildebrand, S. Bultmann, S. Link, K. Thanisch, C. Mulholland, J. Dekker, et al., Spatial organization of transcribed eukaryotic genes, *bioRxiv* (2021).
- [38] G. Fudenberg, M. Imakaev, C. Lu, A. Goloborodko, N. Abdennur, and L. A. Mirny, Formation of chromosomal domains by loop extrusion, *Cell Rep.* **15**, 2038 (2016).
- [39] G. van den Engh, R. Sachs, and B. Trask, Estimating genomic distance from dna sequence location in cell nuclei by a random walk model, *Science* **257**, 1410 (1992).
- [40] S. Sazer and H. Schiessel, The biology and polymer physics underlying large-scale chromosome organization, *Traffic* **19**, 87 (2018).
- [41] S. Plimpton, Fast parallel algorithms for short-range molecular dynamics, *J. Comput. Phys.* **117**, 1 (1995), <http://lammps.sandia.gov>.

Supporting Information

MODEL

We use the well-established model [16], in which the excluded volume interaction between any two monomers is described by a repulsive and shifted Lennard-Jones potential

$$U_{\text{LJ}}(r) = \left(4\epsilon \left[\left(\frac{\sigma}{r} \right)^{12} - \left(\frac{\sigma}{r} \right)^6 \right] + \epsilon \right) \theta(2^{1/6}\sigma - r) \quad (\text{S1})$$

where $\theta(x)$ is the Heaviside step function, σ is the bead's diameter, and ϵ sets the energy scale. As in Ref. [10], the same potential was used for the interaction between monomers and the confining sphere of radius R which was set to achieve an overall monomer density $\rho = 0.85\sigma^{-3}$ (see Tab. S1). The polymer bonds were modeled by a finitely extensible nonlinear elastic (FENE) potential

$$U_{\text{FENE}}(r) = -\frac{1}{2}r_{\text{max}}^2 K \log \left[1 - \left(\frac{r}{r_{\text{max}}} \right)^2 \right], \quad (\text{S2})$$

where $K = 30.0\epsilon/\sigma^2$ and $r_{\text{max}} = 1.5\sigma$. These parameters make the chains essentially noncrossable. We also used the angular bending potential

$$U_{\text{angle}} = k_{\theta}(1 - \cos(\theta - \pi)) \quad (\text{S3})$$

with the parameter $k_{\theta} = 1.5\epsilon$ to induce higher stiffness that corresponds to a lower entanglement length $N_e = 28 \pm 1$ at the studied monomer density ρ [17].

Our simulations start from well-equilibrated configurations of completely passive ring polymer melts in spherical confinement produced in Ref. [10]. Each system contains $M = 46$ ring polymer chains, each of length N ($N = 200, 400, 800$ and 1600 , corresponding to chain entanglement number $Z = N/N_e = 7, 14, 28$ and 57). The choice of $M = 46$ chains was inspired by the 23 pairs of chromosomes in the human diploid cell nucleus, but the main reason is to demonstrate the existence of a topological glass in a small systems to ease future exploration of the phenomenon. At time $t = 0$, the activity was introduced by coupling a consecutive segment of length $N/8$ on each ring to a Langevin thermostat at temperature $T_h = 3.0\epsilon$, whereas the rest of the ring is still maintained at $T_c = 1.0\epsilon$ by another Langevin heat bath. We choose this value of $T_h = 3T_c$, despite the experimental indications of active fluctuations being only about twice the thermal fluctuations. The reason is the heat flux between the active and the passive constituents establishes effective temperatures that are in between the temperatures set by the thermostat. The effective temperatures (measured by the mean kinetic energy) would be the ones measured in the experiments and have the correct ratio about 2 [2]. The equation of motion of the systems were

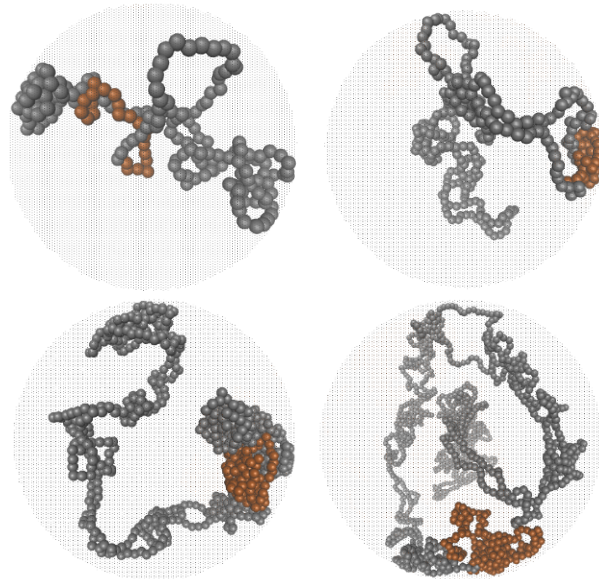


FIG. S1. **Typical conformations of partly active rings in spherical confinement.** The snapshots correspond to $N = 200$ (top left), 400 (top right), 800 (bottom left), and 1600 (bottom right).

integrated using the LAMMPS simulation upackage [41] with the time step $\Delta t = 0.005\tau$ and the damping constant $\gamma = 2/3\tau^{-1}$, where $\tau = \sigma(m/\epsilon)^{1/2}$.

The Langevin thermostat in spherical confinement can induce stochastic values of angular momentum that affect the real dynamics of the system. This effect can be neutralized by zeroing periodically the total angular momentum during the simulations as done in equilibrium simulations in [10]. In the present case, unlike in the equilibrium simulations, we do not perform this operation due to a non-equilibrium character of the studied system as well as potential global flows that can arise in active matter states. When compared to dynamic equilibrium quantities across this work, we also used trajectories produced in a similar fashion without zeroing the angular momentum. We note, however, that the difference in dynamic relaxation times in equilibrium simulations with and without zeroing the angular momentum is rather small.

THREADING DETECTION

We detect the threadings using a minimal surface method that has been used successfully to analyze threading constraints for systems containing ring polymers in equilibrium [10, 20, 22] and out of equilibrium [1, 2, 21]. The essence of the method is an unambiguous definition of the threading as the intersection of a rings

N	N_h	R/σ	$\langle R_g^2 \rangle / \sigma^2$	$\langle R_{ee}^2 \rangle / \sigma^2$	$\langle R_{ee}^2 \rangle / \langle R_g^2 \rangle$	$\langle \lambda_1 \rangle / \langle \lambda_3 \rangle$	$\langle \lambda_2 \rangle / \langle \lambda_3 \rangle$	$\langle R_g^2 \rangle / R^2$	$\langle R_{ee}^2 \rangle / R^2$
200	25	13.72	62.4(0.7)	164.8(6.2)	2.64	12.0(0.7)	4.3(0.2)	0.33	0.87
400	50	17.29	129.3(0.6)	304.4(6.2)	2.34	6.5(0.4)	3.1(0.7)	0.41	1.01
800	100	21.78	227.7(0.5)	468.6(3.1)	2.05	4.6(0.2)	2.7(0.8)	0.47	0.98
1600	200	27.44	376.1(0.7)	810.8(4.7)	2.15	3.5(0.5)	2.2(0.1)	0.49	1.07

TABLE S1. **Size and shape properties of partially active rings in a confining sphere.** The mean values as well as their standard errors (indicated in the parentheses) were estimated in the steady states. R is the radius of the sphere. $\langle R_g^2 \rangle$ and $\langle R_{ee}^2 \rangle$ are the mean-square radius of gyration and the mean-square spanning distance between monomers $N/2$ apart, respectively. λ_i ($i = 1, 2, 3$, $\lambda_1 \geq \lambda_2 \geq \lambda_3$) are the eigenvalues of the gyration tensor.

N	N_h	$\langle R_g^2 \rangle / \sigma^2$	$\langle R_e^2 \rangle / \sigma^2$	$\langle R_{ee}^2 \rangle / \langle R_g^2 \rangle$	$\langle \lambda_1 \rangle / \langle \lambda_3 \rangle$	$\langle \lambda_2 \rangle / \langle \lambda_3 \rangle$
100	13	18.1(0.1)	54.9(0.1)	3.0	7.3(0.1)	2.34(0.01)
200	25	65.2(0.3)	203.5(3.8)	3.1	12.4(0.1)	2.81(0.01)
400	50	182.1(0.7)	566.1(2.1)	3.1	14.2(0.2)	3.03(0.02)

TABLE S2. **Size and shape properties of the partially active rings in bulk.** $\langle R_g^2 \rangle$ is the mean-square radius of gyration, $\langle R_e^2 \rangle$ is the mean-square distance between two monomers separated by the contour length $N/2$, and λ_i , $i = 1, 2, 3$ are the eigenvalues of the gyration tensor ordered such that $\lambda_1 \geq \lambda_2 \geq \lambda_3$. The value in the parentheses indicates the standard error. For comparison with equilibrium values, please see Table S3. Adapted from Ref. [2].

N	R/σ	$\langle R_g^2 \rangle / \sigma^2$	$\langle R_e^2 \rangle / \sigma^2$	$\langle R_{ee}^2 \rangle / \langle R_g^2 \rangle$	$\langle \lambda_1 \rangle / \langle \lambda_3 \rangle$	$\langle \lambda_2 \rangle / \langle \lambda_3 \rangle$
200	13.72	26.4(0.2)	73.4(0.6)	2.8	5.64(0.04)	2.25(0.01)
400	17.29	44.4(0.7)	120.7(2.5)	2.7	5.24(0.08)	2.14(0.02)
800	21.78	73.1(1.1)	195.4(3.8)	2.7	4.93(0.10)	2.06(0.01)
1600	27.44	120.5(2.8)	320.2(10.4)	2.7	4.89(0.12)	2.03(0.02)

TABLE S3. **Size and shape properties of the equilibrium confined rings.** R is the radius of the confining sphere, $\langle R_g^2 \rangle$ is the mean-square radius of gyration, $\langle R_e^2 \rangle$ is the mean-square distance between two monomers separated by the contour length $N/2$, and λ_i , $i = 1, 2, 3$ are the eigenvalues of the gyration tensor ordered such that $\lambda_1 \geq \lambda_2 \geq \lambda_3$. The value in the parentheses indicates the standard error. Adapted from Ref. [10]

contour with a disk-like surface spanned on another ring. As there are many possible surfaces with the contour of the ring a surface of minimal surface area is chosen. For the details on practical implementation of the algorithm we refer the reader to [1, 21]. The reported value of number of threaded neighbors n_{tn} is a mean number of rings each ring threads as in [1].

ADDITIONAL CONFORMATIONAL PROPERTIES

In Fig. S2 we report additional conformational properties of the rings. There we compare scaling of the gyration radius in the present active confined system with the bulk and the equilibrium counterparts. Additionally we show the profile of the contact probability and the scaling of the mean square internal distance that exhibits the self-avoiding statistics.

MEAN-SQUARE DISPLACEMENTS

We compute the mean-squared displacement $g_3(t)$ as

$$g_3(t, t_0, t_{tot}) = \left\langle \frac{1}{t_{tot} - t} \int_{t_0}^{t_0 + t_{tot} - t} [\mathbf{R}(t' + t) - \mathbf{R}(t')]^2 dt' \right\rangle \quad (S4)$$

where t_0 is the initial time point chosen as the onset of the steady state ($3 \cdot 10^6 \tau$ in case of active rings and 0 for equilibrium), t_{tot} is the total simulation time, \mathbf{R} is the position of the ring's center of mass with respect to the global center of mass and the angles mean averaging over different rings.

Additionally, we compute the relative mean-square distance $g_{3,rel}(t)$:

$$g_{3,rel}(t) = \left\langle \frac{1}{t_{tot} - t} \int_{t_0}^{t_0 + t_{tot} - t} [d_{ij}(t' + t) - d_{ij}(t')]^2 dt' \right\rangle_{ij} \quad (S5)$$

where t_0 and t_{tot} are as above, d_{ij} is the relative *distance* between rings i and j and the $\langle \dots \rangle_{ij}$ is the average over all possible ring pairs in the system.

SPATIO-TEMPORAL CORRELATIONS

The spatio-temporal correlations are computed similarly to [12, 14] as

$$C_s(r; \Delta t) = \left\langle \frac{\sum_{i>j} [\Delta \mathbf{R}_i(t, \Delta t) \cdot \Delta \mathbf{R}_j(t, \Delta t)] \delta(\mathbf{R}_{ij} - r)}{\sum_{i>j} \delta(\mathbf{R}_{ij} - r)} \right\rangle \quad (\text{S6})$$

where $\Delta \mathbf{R}_i(t, \Delta t)$ is the displacement of the i -th monomer in lag time Δt as measured in time t . The angular brackets represent averaging over time, in the active case only over the steady state. In the active system, the correlation decays significantly slower in com-

parison to equilibrium and there is a strong anticorrelation at longer lag times at the opposing positions in the spherical confinement ($r \simeq 1.5R$) (Fig. S3a). In part, this is a consequence of the Langevin dynamics that induces stochastic angular momentum also in equilibrium (Fig. S3b). However, the anticorrelation is much more pronounced in the active topological glass state, and almost nonexistent in equilibrium with zeroed angular momentum (Fig. S3c). We observe larger correlation length for the active case consistent with [12, 15, 27], but in contrast to [14]. However, the correlation length seems to be monotonically increasing and saturating with time that is consistent with some cases in [27], but non-monotonic correlation length has been observed in other cases at longer time lags [12, 14, 15, 27].

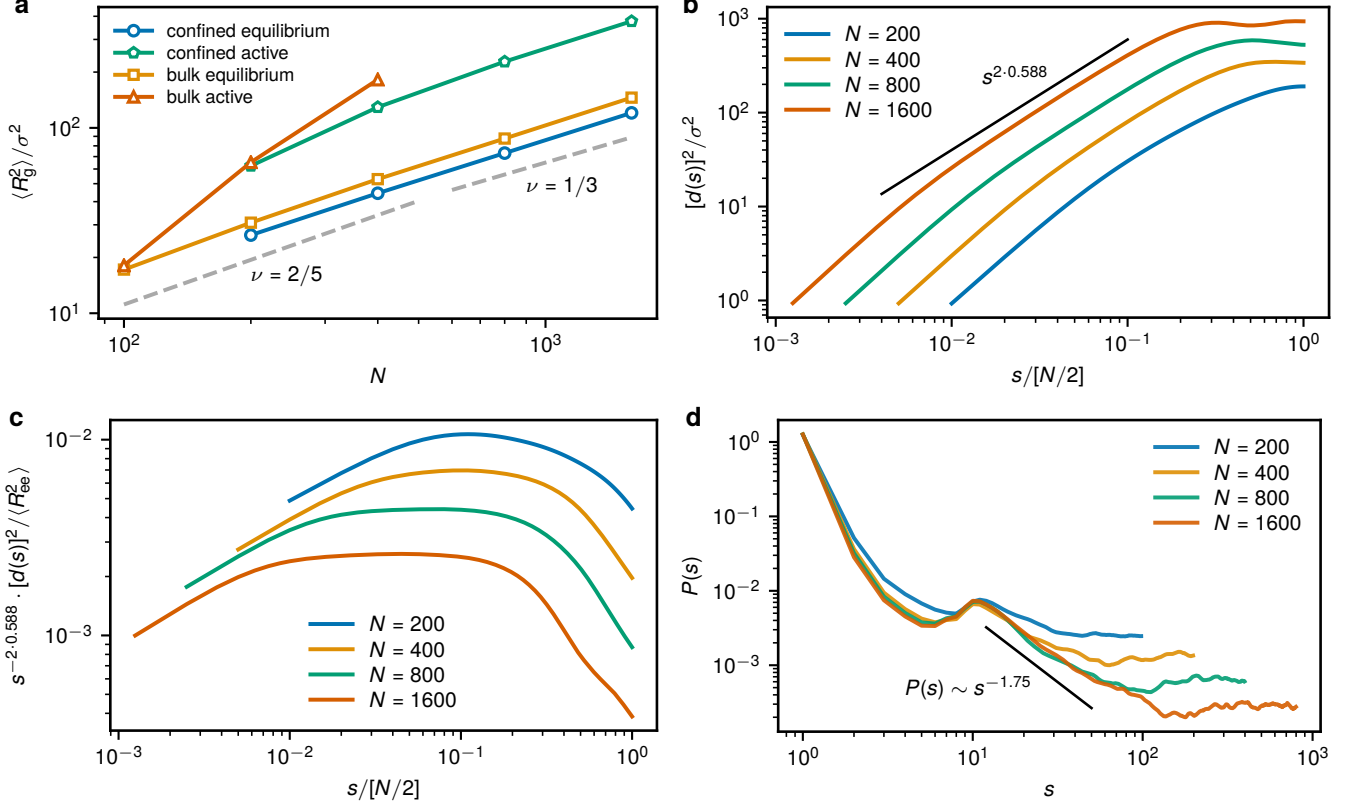


FIG. S2. **Additional conformational properties.** **a**, Comparison of the scaling of the radius of gyration with the ring length for different systems. The confined active rings are from the present work, the confined equilibrium rings are from [10], the bulk equilibrium are from [17], and the bulk active rings from [1]. The equilibrium scaling exponent $\nu = 1/3$ is shown as well as the crossover with “effective exponent” $2/5$. The seeming compact scaling of the active confined rings is not due to their internal structure (see **b**), but just because the confining radius R scales with $N^{1/2}$ as the systems of different N were simulated with the same number of chains and the same density. **b**, The mean-square internal-distance $d(s)$ is computed as the mean square end-to-end vector of a segment of length s averaged over its position within a ring and over different rings in the steady state. In the intermediate distances ($s/(N/2) \in [10^{-2}; 10^{-1}]$) we recover self-avoiding walk scaling exponent 0.588 for the longer ($N \geq 400$) rings. These exhibit also monotonic profile for large contour distances. **c**, The mean-square internal-distance $d(s)$ rescaled by the $s^{0.588}$. The broadening plateau for the rings of $N \geq 400$ shows the asymptotic self-avoiding regime. **d**, The contact probability $P(s)$ is the probability of finding the endpoints of a segment s at distance below $2^{1/6}\sigma$. It is an average over the segment’s position within a ring and over different rings in the steady state. At intermediate distances and for long rings we recover exponent γ close to 1.75 consistent with the self-avoiding random walk configuration. At longer lengths, $P(s)$ goes to a constant signifying the positional decorrelation due to reflections from the wall — this is typical profile of an equilibrium globule, i.e. confined melt of linear chains. The exponent γ is smaller for shorter rings. The non-monotonic character is due to the phase separation of the hot and cold segments and the doubly-folded structure.

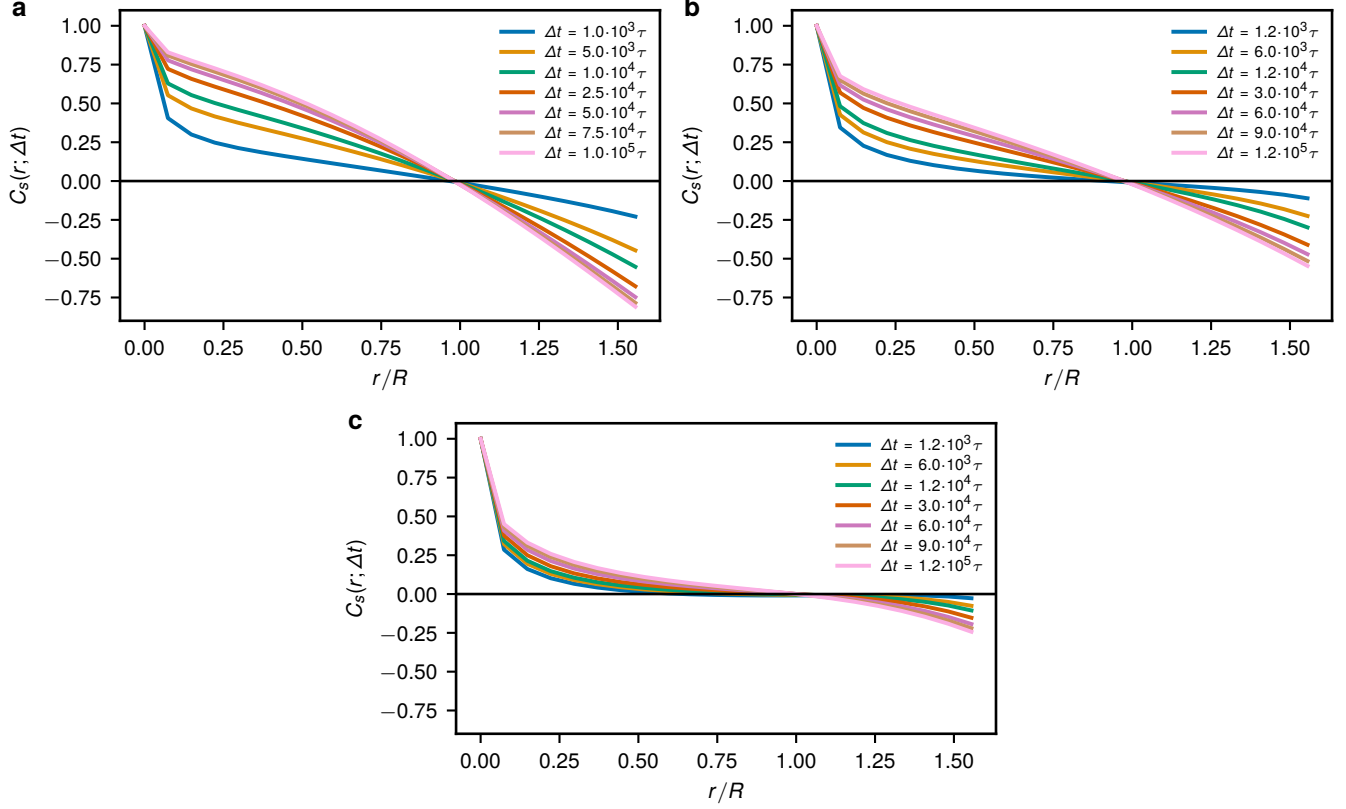


FIG. S3. **Spatio-temporal displacement correlation.** The correlation for $N = 200$ system computed by (S6) for **a** the active confined rings, **b** equilibrium rings without zeroing the angular momentum, **c** equilibrium rings with zeroing the angular momentum from Ref. [10].